Journal of
Marine Science and Engineering

MDPI

Article

Experimental Study on Unsteady Cavitating Flow and Its Instability in Liquid Rocket Engine Inducer

Hao Wang [1], Jian Feng [1], Keyang Liu [1], Xi Shen [1], Bin Xu [1,*], Desheng Zhang [1,*] and Weibin Zhang [2]

[1] Research Center of Fluid Machinery Engineering and Technology, Jiangsu University, Zhenjiang 212013, China; 2222011052@stmail.ujs.edu.cn (H.W.); fengj0625@sina.com (J.F.); 2212011018@stmail.ujs.edu.cn (K.L.); x.shen@ujs.edu.cn (X.S.)
[2] Key Laboratory (Fluid Machinery and Engineering Research Base) of Sichuan Province, Xihua University, Chengdu 610039, China; zhangwb@mail.xhu.edu.cn
* Correspondence: norkistar@ujs.edu.cn (B.X.); zds@ujs.edu.cn (D.Z.)

Abstract: To study instability in the unsteady cavitating flow in a liquid rocket engine inducer, visualization experiments of non-cavitating and cavitating flows inside a model inducer were carried out at different flow conditions. Visual experiments were carried out to capture the evolution of non-cavitating and cavitating flows in a three-bladed inducer by using a high-speed camera. The external characteristic performance, cavitation performance, and pressure pulsation were analyzed based on the observation of non-cavitation and cavitation development and their instabilities. Under non-cavitation conditions, the change of flow rate has a significant impact on the pressure pulsation characteristics in the inducer. The occurrence of cavitation aggravated the instability of the flow and caused the intensity of pressure pulsation at each measuring point to increase. This cavitation structure has strong instability, and the tail region is often accompanied by shedding cavitation clouds perpendicular to the blade surface.

Keywords: liquid rocket engine; inducer; cavitating flow; instability; experiment

check for updates

Citation: Wang, H.; Feng, J.; Liu, K.; Shen, X.; Xu, B.; Zhang, D.; Zhang, W. Experimental Study on Unsteady Cavitating Flow and Its Instability in Liquid Rocket Engine Inducer. *J. Mar. Sci. Eng.* **2022**, *10*, 806. https://doi.org/10.3390/jmse10060806

Academic Editor: Kourosh Koushan

Received: 5 May 2022
Accepted: 10 June 2022
Published: 12 June 2022

1. Introduction

High-thrust liquid rocket engines (LREs) not only power next-generation launch vehicles, but also the main propulsion systems for many space activities, such as manned lunar landings and deep space exploration [1–5]. The turbopump is the core component of the liquid rocket engine. The high rotation speed and low inlet pressure make the turbopump prone to cavitation at the inlet [6]. In the aerospace industry, to improve the cavitation performance of the turbopump, it is common to install an inducer at the front of the turbopump [7]. The inducer (due to its characteristics of having long blade flow paths and small installation angles) has good cavitation performance and can work under certain cavitation conditions [8]. The flow instability induced by cavitation has been one of the main sources of LRE vibration for a long time, and it has severely restricted the improvement of LRE performance and reliability in the aerospace field [9,10].

Although there is research on the flow instability induced by cavitation [11], the characteristics of flow instability induced by cavitation in the inducer still need to be further explored. Since cavitation involves complex phenomena, such as turbulence [12], phase transition [13], and two-phase flow [14], it is difficult to achieve the expected research goals through theoretical analyses and numerical simulations; experiments are still the best research methods. One of the most important problems encountered in improving credible inducers for turbopumps involves the instability of the cavitating flow [15] in the centrifugal pump [16]. The instability of the cavitating flow can induce complicated flow structures and unsteady pressure pulsations, damaging the pump components. Therefore, it is necessary to understand the characteristics of the external characteristic performance, cavitation performance, pressure pulsation, and flow pattern caused by non-cavitating and cavitating flow-induced instabilities.

Many researchers have focused on non-cavitating and cavitating flows and instabilities in inducers. Some experimental studies have been carried out to investigate these instabilities. Lee et al. [17] employed a two-blade inducer to investigate the cavitation instability. Asymmetric cavitation and cavitation surge were observed. Kim and Song [18] designed a water test facility for the cavitation experiment of a turbopump inducer. Non-cavitation and cavitation performances were studied to have a basic understanding of the inducer cavitation. Different types of cavitation were identified. Cui et al. [19] analyzed the evolution of cavitation in a low-specific high-speed centrifugal pump with an inducer, based on experimental and numerical studies. Different types of cavitation, such as sheet cavitation, cloud cavitation, and tip leakage vortex cavitation, were observed in the blade passage of the inducer. It was found that asymmetric cavitation occurred when the net positive suction head was lower. Meanwhile, the bubble blocked the flow passage of the inducer, resulting in a decrease in the head and efficiency. Followed by previous work, Cui and Chen [20] performed a numerical simulation analysis to study these instabilities from the view of vapor volume fraction and blade loading. Backflow cavitation appeared in the upstream region of the inducer at a critical cavitation number. Moreover, a cavitation surge was observed in the experiment. Li et al. [21] investigated the cavitating and non-cavitating flows in a rocket engine inducer. Cavitation images were obtained based on the experimental study. This study could be potentially used as a reference for the cavitating flow in the rocket engine inducer due to the cavitation images and dynamic pressure impulse obtained on the experimental platform. Xiang et al. [22] conducted several experimental studies to investigate the development of cavitation and pressure variations in an inducer. Zhang et al. [23] studied the cavitation performance of an inducer and its modifications, experimentally and numerically. Cavitation performance and hydraulic efficiency were found to be dependent on the inlet blade angle. Cheng et al. [24] experimentally investigated the influence of the annular groove position on the cavitation performance of a high-speed inducer. The results indicate that the annular groove has an axial optimal position in suppressing the cavitation instability. Xu et al. [25] experimentally studied the cavitation characteristics of an inducer under low flow conditions. A band-shaped backflow vortex was found when the flow rate was very low. Huan et al. [26] studied cavitation evolution in a high-speed centrifugal pump with an inducer. A typical evolution process of the cavitation was obtained, including the inception, the development, and the deterioration. Zhang et al. [27] investigated cavitation behavior in a high-speed inducer with a great flow rate. When the cavitation number decreased, the vortex cavitation was induced along with the tip leakage vortex; subsequently, wedge-shaped sheet cavitation occurred, followed by backflow vortex cavitation. Based on the reports from the above researchers, a systematic analysis of the external characteristic performance, cavitation characteristic curve, pressure pulsation, and cavitation patterns need to be constructed.

This paper studied the non-cavitation and cavitation instabilities of a three-blade inducer by conducting visual experiments at different flow rates. The experimental setup and method are described in Section 2. The results and discussions are illustrated in Section 3, including the external characteristic performance, cavitation characteristic curve, pressure pulsation characteristics, and a high-speed photography experiment analysis. Finally, the conclusions are summarized in Section 4.

2. Experimental Setup and Method

2.1. Geometry of Inducer

This research used an inducer as the research object; the flow-passing parts were the inlet pipe, the inducer, the support plate, the elbow, and the outlet pipe, respectively. The structure of the inducer is shown in Figure 1. The specific parameters of the inducer are shown in Table 1.

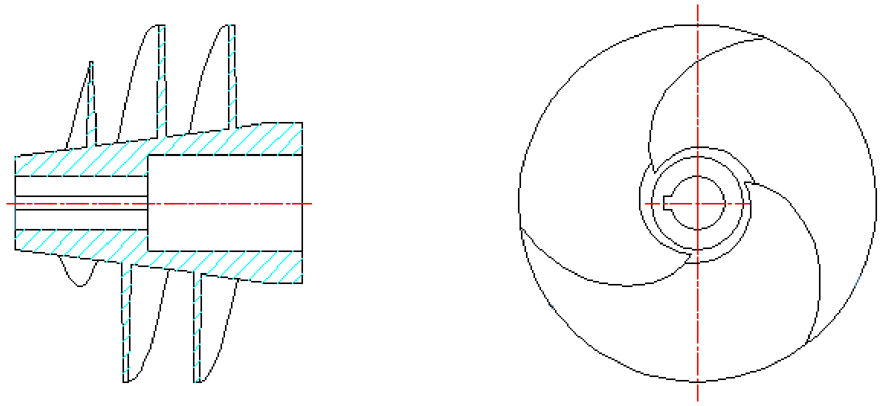

Figure 1. Structure of the inducer.

Table 1. Design parameters of the inducer.

Parameter	Value
Design discharge $Q_d/(m^3/h)$	159.12
Rotation speed $n/(r/min)$	1450
Inlet diameter D_t/mm	199
Hub diameter at leading-edge d_{h1}/mm	51
Hub diameter at leading-edge d_{h2}/mm	90
Inlet tip blade angle $\beta_{t1}/°$	10.7
Wrap angle at leading-edge $\Delta\varphi/°$	128
Cascade solidity s	2.1
Number of blades z	3
Tip gap d_1/mm	0.5

2.2. Experimental Setup

The external characteristic performance, cavitation performance, pressure measurement, and high-speed photography were performed in a closed experimental system at the National Fluid Machinery Laboratory, Jiangsu University. The main components of the experimental system are illustrated in Figure 2, consisting of 1—motor, 2—torque meter, 3—experimental pump, 4—runner chamber, 5—gate valve, 6—stabilizing tank, 7—regulating valve, 8—flow meter, 9—booster pump, 10—outlet pressure sensor, 11—inlet pressure sensor.

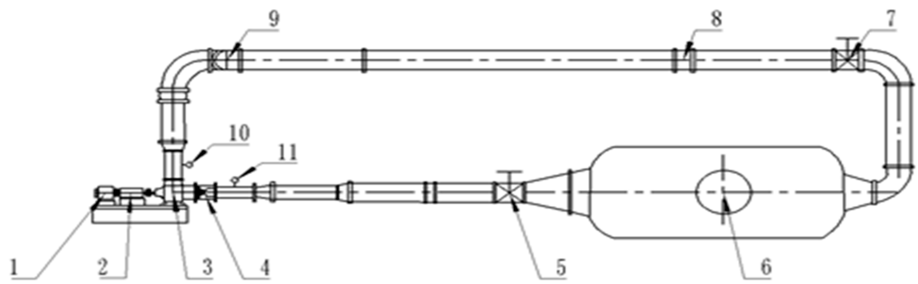

Figure 2. Schematic illustration of the experimental system.

2.3. Experimental Method

2.3.1. Experimental Method for the External Characteristic Performance

For the first step, idle the motor to adjust the torque to be zero before connecting with the drive shaft. In this experiment, the valve at the outlet section is used to change the flow rate in the circulation pipeline, and the valve at the inlet section should be adjusted to a fully open state. This approach is used to prevent the unstable flow generated by the sudden change of the inlet pipeline from interfering with the flow field at the inlet of the inducer. To change the value of the flow rate in the pipeline, the position of the valve at the outlet is adjusted. After the flow in the pipeline is stable, the pressure and torque data are to be recorded; the above operation is to be repeated to obtain data under different flow conditions.

2.3.2. Experimental Method for Cavitation Performance

A cavitation tank is placed above a water tank. Half of this cavitation tank contains water and the other half contains air. A vacuum pump is connected to the cavitation tank to adjust the inlet pressure of the inducer to obtain different cavitation performances. When the inlet pressure of the inducer is reduced to the specified value, the pressure data at the outlet is to be recorded; the above operation is to be repeated to obtain the cavitation performances under different flow conditions.

2.3.3. Experimental Method for Pressure Pulsation

The installation position of the pressure sensor is shown in Figure 3. There are four pressure measuring points in the experiment, which are located at P1 (the inlet of the inducer), P4 and P6 (the middle of the inducer), and P7 (the outlet of the inducer). P2, P3, and P5 are not used in the experiments. Pressure sensors (PCB 113B28) are employed to measure the pressure on each measuring location. The measuring range of PCB 113B28 is between 0.69 and 690 kPa. The resonant frequency FR is set to be 500 kHz, while low frequency (−5%) FL is set to be 0.5 Hz. The sampling frequency is set to be 1024 Hz.

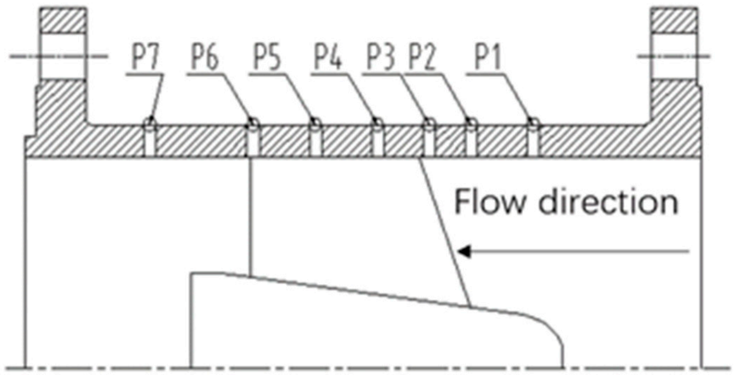

Figure 3. Schematic illustration of pressure monitors (P1–P7 are the measuring points).

2.3.4. Experimental Method for High-Speed Photography

With the help of high-speed photography technology, a variety of flow details can be clearly captured to reveal the variations of the cavitation, vortex, etc. To enable the high-speed camera to capture the flow in the inducer, a transparent sleeve made of plexiglass was used as the runner chamber in the experiment, as shown in Figure 4. The high-speed photography experiment device is mainly composed of a high-speed camera, image display, and fill light. The layout of the experimental device is shown in Figure 5. Considering that the rotational speed of the inducer is 1450 r/min, the shooting frequency of the high-speed camera in this experiment is set at 4000 Hz to capture variations of the flow field.

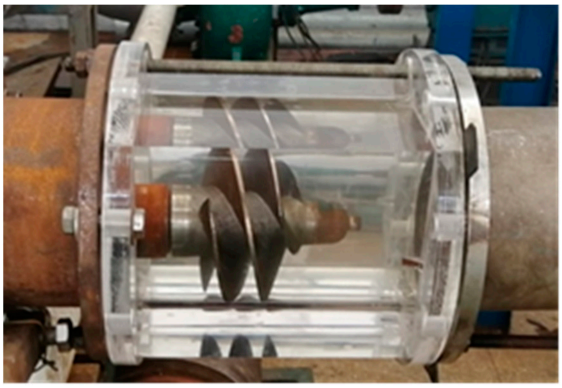

Figure 4. Transparent sleeve.

Figure 5. Layout of the experimental device.

2.4. Uncertainty Analysis

The experimental uncertainty U_v mainly consists of systematic uncertainty U_{sys} and stochastic uncertainty U_{sto}, defined as follows,

$$U_v = \sqrt{U_{sys}^2 + U_{sto}^2}. \tag{1}$$

The systematic uncertainty U_{sys} is determined by the residual uncertainty of the experimental instruments and methods, while the stochastic uncertainty U_{sto} is determined by the uncontrolled experimental conditions. The experimental uncertainty is about 0.4%.

3. Results and Discussions

3.1. External Characteristic Performance

The external characteristic performance curve obtained by the experiment is shown in Figure 6. Figure 6a shows the performance characteristic curve of the inducer head in the flow rate Q/Q_d ranging from 0.2 to 1.2. The head characteristic curve shows a gradually decreasing trend with the flow rate, indicating that the hydraulic performance of the inducer is relatively good. Figure 6b shows the performance characteristic curve of the inducer efficiency in the flow rate Q/Q_d ranging from 0.2 to 1.2. The efficiency characteristic curve shows a gradually increasing trend with the flow rate Q/Q_d ranging from 0.2 to 1.0. The inducer efficiency considerably decreases when the flow rate Q/Q_d exceeds 1.0. The inducer efficiency reaches the peak value in the flow rate Q/Q_d = 1.0, which shows that the 1.0 Q_d working condition is the optimal working condition of the inducer. In the optimal working condition, the head is 2.13 m, and the efficiency is 48.7%.

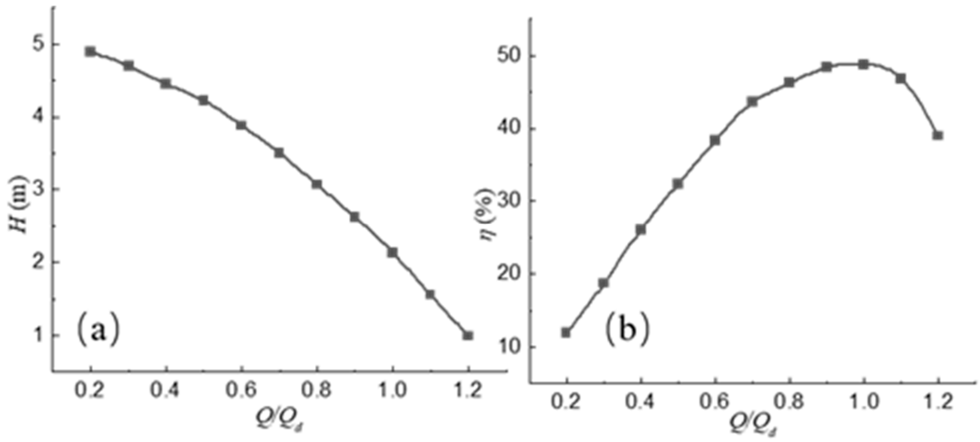

Figure 6. External characteristic curve of inducer: (**a**) head performance curve; (**b**) efficiency performance curve.

3.2. Cavitation Characteristic Curve

Cavitation performance experiments can quantitatively reflect the anti-cavitation performances of the inducers. In this paper, cavitation performance experiments under various working conditions were carried out, and the cavitation characteristic curve of the inducer was drawn based on the experimental results, as shown in Figure 7. It can be seen from the figure that under different flow conditions, the trend of the cavitation characteristic curve of the inducer is different. In the 0.6 Q_d working condition, as the *NPSHa* decreases, the head rises slowly, while in the 0.8 Q_d working condition, there is an opposite trend. In the 1.1 Q_d working condition, compared with the 0.6 Q_d and 0.8 Q_d working conditions, the cavitation characteristic curve is almost flat, which means that the inducer has a strong anti-cavitation ability in large flow working conditions.

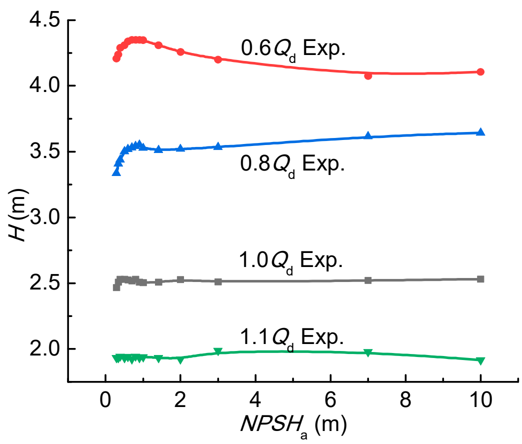

Figure 7. Cavitation performance of the inducer under different flow conditions.

3.3. Pressure Pulsation Characteristics Analysis

To facilitate the comparison of the pressure pulsation characteristics in various working conditions, the pressure data obtained in the experiment is converted into a dimensionless pressure pulsation coefficient C_p, the expression is as follows:

$$C_p = \frac{p - \overline{p}}{0.5\rho_l U_t^2} \tag{2}$$

where p is the pressure, $\overline{p}$ the time averaged pressure, ρ_l is the liquid density, U_t is the rim speed.

3.4. Non-Cavitation Condition

3.4.1. Time Domain Analysis

Figure 8 shows the time domain variations of the pressure pulsation for the 0.6 Q_d, 1.0 Q_d, and 1.1 Q_d flow conditions under non-cavitation conditions. In Figure 8, the abscissa N represents the number of cycles, and the expression is as follows,

$$N = \frac{t}{T_{\mathrm{rev}}} \tag{3}$$

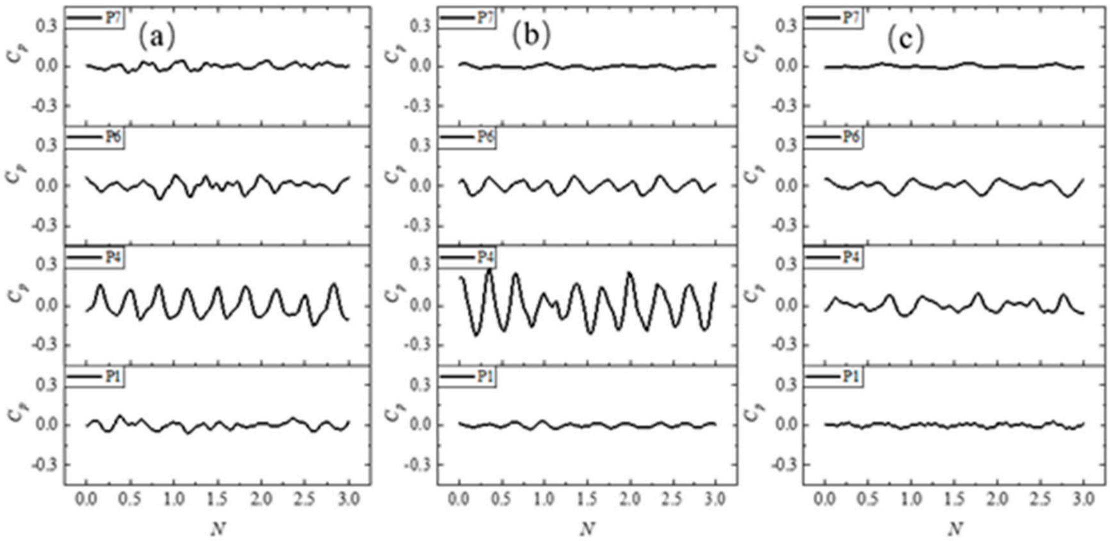

Figure 8. Time domains of pressure fluctuations under different flowrate conditions: (**a**) 0.6 Q_d; (**b**) 1.0 Q_d; (**c**) 1.1 Q_d.

In the formula, t represents the collection time of the pressure value and T_{rev} represents the time for the inducer to rotate for one cycle.

Comparing and analyzing the pressure pulsation in each flow condition, it can be found that in one rotation period, the pressure pulsation curve has three crests and troughs, which correspond to the three blades of the inducer. Obviously, the amplitude of the pressure pulsation at the measuring point P4 is much larger than the amplitude at the other three measuring points. This is because the position of the measuring point P4 locates in the work area of the blade. With the rotation of the inducer, the blade sweeps across the measuring point P4, and the liquid at that place is pressurized instantaneously, resulting in large fluctuations in the pressure.

The pressure pulsation at the measuring point P1 (at the inlet of the inducer) is messy in the low flow rate of 0.6 Q_d. The pressure pulsation amplitude in each rotation period has a certain difference. In small flow conditions, the more significant pressure difference between the suction surface and the pressure surface of the blade causes the tip leakage flow to move further upstream of the inducer, where it interacts with the main flow, and a backflow vortex is formed under the action of the shearing force, which destroys the continuity of the liquid flow there, causing flow turbulence. With the increase of the flow rate, in the design flow rate of 1.0 Q_d, it can be observed that the pressure pulsation at the measuring point P1 has a strong periodicity. Although there are certain fluctuations, it is relatively stable, and the amplitude is relatively small. When the flow rate increases to 1.1 Q_d, the pressure pulsation amplitude continues to decrease, and multiple secondary peaks appear at the peak position, which may be caused by the effect of the tip leakage vortex.

The pressure pulsation at the measuring point P4 located in the middle of the inducer shows a strong periodicity at a low flow rate of 0.6 Q_d, similar to a sinusoidal oscillation.

When the flow rate increases to the design flow rate of 1.0 Q_d, the period of the pressure pulsation will be weakened to a certain extent, the amplitude of the pressure pulsation will decrease to a certain extent in the second period, and there will be a more obvious secondary peak. In the high flow rate of 1.1 Q_d, the periodicity of the pressure pulsation is further weakened. The waveforms in the first and second cycles are similar, but the peaks of the various peaks are inconsistent, showing a step change; a larger one and two similar peaks appear in the third cycle.

The measurement point P6 is located at the trailing edge area of the inducer blade. Comparing the pressure pulsation curves in the three flow conditions—in the 0.6 Q_d operating condition, there are secondary peaks and the peak and valley values of each cycle are different, showing that the flow field is more complicated in the small flow conditions, which leads to irregular fluctuations in the pressure pulsation. When the flow reaches a 1.0 Q_d working condition, the pressure pulsation changes periodically, showing the characteristics of sinusoidal change, indicating that the inducer runs more stable and the hydraulic performance is better in the design flow working condition. In the 1.1 Q_d working condition, there are two larger peaks and two similar secondary peaks in one cycle. This shows that in large-flow conditions, there is a large-scale vortex in the exit area of the inducer, but the shape and movement of the vortex are relatively stable.

From the change of the pressure pulsation curve at the measuring point P7, it can be seen that although the position of the measuring point P7 is far away from the working area of the inducer, there is no rectifying structure downstream of the inducer, and the liquid flowing out of the inducer maintains a large amount of circulation. It rotates and flows at a high speed around the central axis of the inducer, so the pressure pulsation at the measuring point fluctuates irregularly, especially in the off-working condition. In the design flow conditions, the pressure pulsation amplitude is very small and the pulsation curve is generally flat, indicating that the flow is relatively stable in the design flow conditions, and there is no large-scale vortex.

3.4.2. Frequency Domain Analysis

Figure 9 shows the pressure pulsation frequency domain diagrams at the pressure pulsation measuring points P1, P4, P6, and P7 in different flow conditions. The abscissa NF in the figure represents the 'multiple shaft frequency', which is expressed as,

$$N_F = \frac{60f}{n} = \frac{f}{f_n} \tag{4}$$

In the formula, f represents the frequency obtained by the Fourier transform and f_n represents the shaft frequency.

Comparing and analyzing the frequency domain characteristics of the three flow conditions—it can be found that the main frequency at the measurement point P4 is always three times the shaft frequency (that is, the blade passage frequency, which is the passage frequency of the blade). This is because the inducer has three blades. At the same time, the high-order harmonics of the leaf frequency can be observed, such as the '6-multiple shaft frequency', where the pulsation amplitude is second only to the pulsation amplitude corresponding to the main frequency. In addition, the amplitude of the main frequency increases first and then decreases with the increase of the flow rate, which is the largest in the design flow condition but drops significantly in the large flow condition. The main frequencies of the pressure pulsations of the remaining three measuring points (P1, P6, and P7) are the blade passage frequencies in the flow rates of 0.6 Q_d and 1.0 Q_d (the corresponding amplitudes of the main frequencies are similar). However, in the high flow rate of 1.1 Q_d, the main frequencies at the three measuring points all shifted to the low-frequency directions (located at two times the shaft frequency). The amplitude corresponding to each frequency at P7 is much smaller than the frequency at the other three measuring points, especially in the large flow condition. The amplitude corresponding to the frequency that is higher than the leaf frequency is close to zero. This is because the axial distance between the P7 measuring point and the work area of the inducer is relatively large. At the same time, there are multiple low-frequency components at each measuring point in the low flow rate of 0.6 Q_d, and the low-frequency pulsation intensity is relatively large. As the flow rate increases, the pulsations of these low-frequency components gradually weaken. The pulsations of these low-frequency components basically disappear in the large-flow conditions. These low-frequency components come from the influence of large-scale vortices, such as the tip leakage vortex and backflow vortex in the flow field. In small flow conditions, these vortices have wide distribution areas and greater impacts on the stability of the flow.

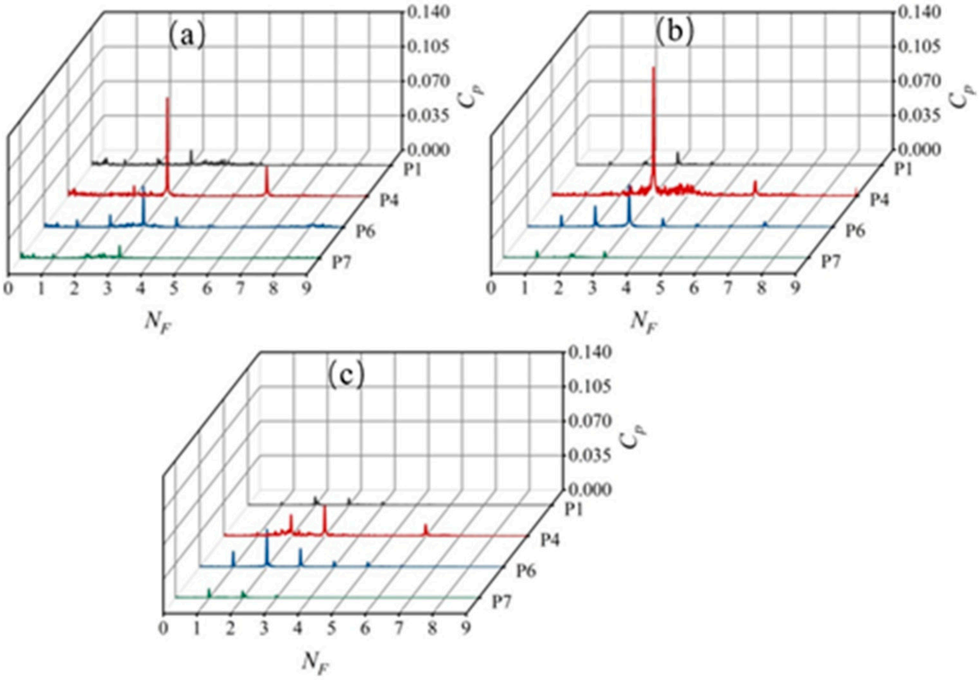

Figure 9. Frequency domains of pressure fluctuations under different flowrate conditions: (**a**) 0.6 Q_d; (**b**) 1.0 Q_d; (**c**) 1.1 Q_d.

3.5. Cavitation Condition

3.5.1. Time Domain Analysis

To study the pressure pulsation characteristics at different inducer positions (under cavitation conditions), a time domain diagram of the pressure pulsation in different *NPSHa* (5.51, 4.28, 3.05, and 1.82 m) at a design flow rate of 1.0 Q_d is illustrated in Figure 10.

When the *NPSHa* is 5.51 m, as shown in Figure 10a, the degree of cavitation is not obvious, the flow in the inducer is relatively stable, and the periodicity of the pressure change curve can be observed. The pressure pulsation curve at the measuring point P1 has large fluctuations, indicating that the cavitation area in the inducer developed to the upstream area at this time, and the formation and collapse of the cavitation process caused the pressure pulsation at this place to increase. This means that pressure pulsation can be employed to predict the development of the cavitation area.

With the further decrease of inlet pressure, when the *NPSHa* is 4.28 m, as shown in Figure 10b, the degree of cavitation increases, and the gas volume fraction increases, which is reflected in the strong fluctuation of the pressure pulsation at the measuring point P1. At the same time, there is only one wave crest in a cycle, indicating that the cavitation has a greater effect on pressure pulsation. For the measuring point P6, the pressure pulsation at this point presents a strong periodicity, but the amplitude changes stepwise within one rotation period. This may be due to the collapse of cavitation at this point, resulting in a sudden increase in the amplitude of the pressure pulsation.

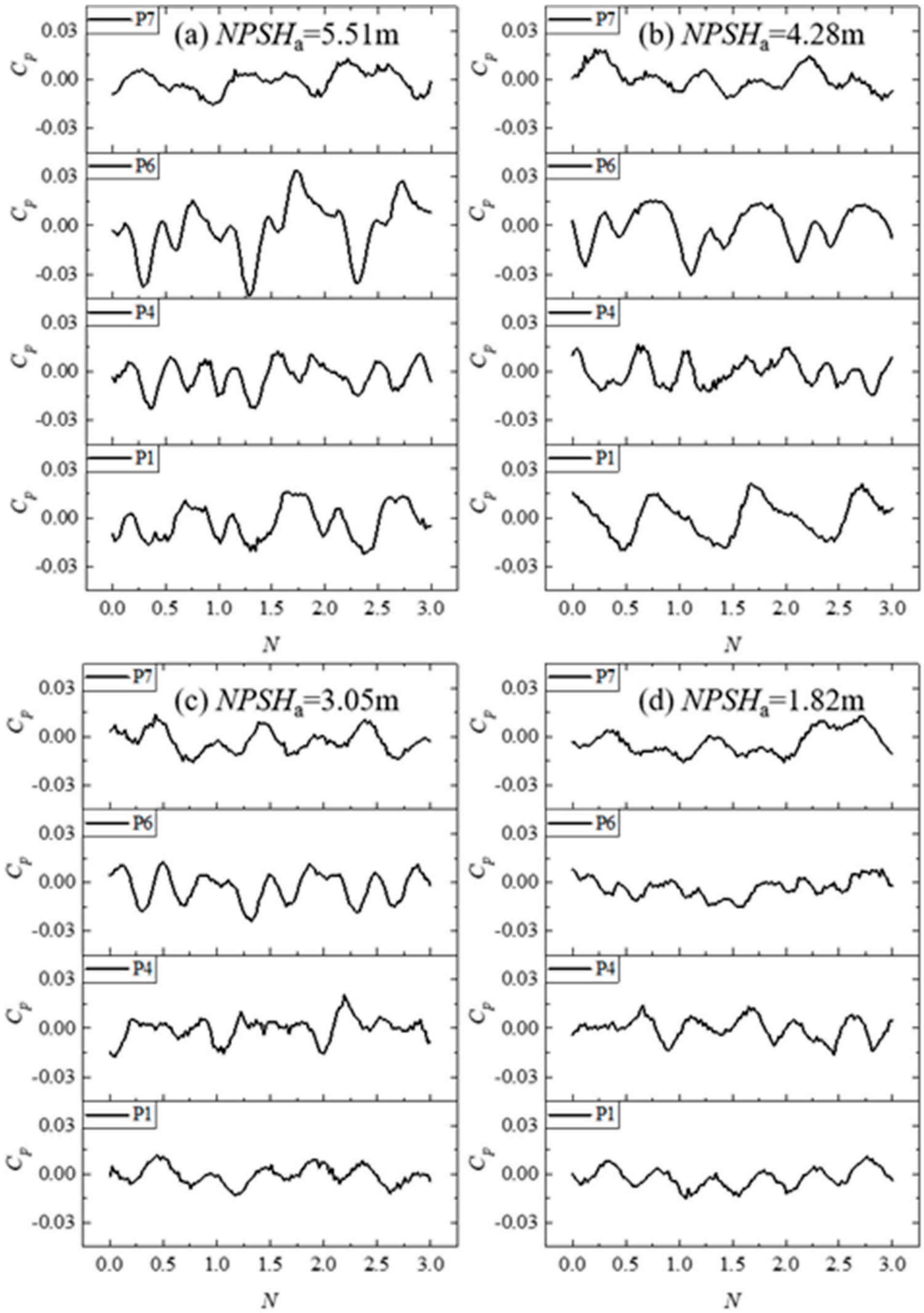

Figure 10. Time domains of pressure fluctuations under different *NPSHa*.

When the *NPSHa* is 3.05 m as shown in Figure 10c, the difference between the peak and valley values of the pressure pulsation at the inlet of the inducer is significantly reduced. It is worth noting that the pressure pulsation curve of measuring point P4 is special. In one rotation period, the pressure pulsation curve first rises rapidly, then fluctuates at a small amplitude near zero amplitude, and finally declines rapidly, showing a change similar to a rectangular wave. This indicates that the leading-edge area of the tip of the inducer blade is filled with a large number of bubbles, and the cavitation degree on the three blades is not completely the same. The pressure at the measuring point P4 appears to remain stable for a short time and then drops rapidly.

When the *NPSHa* is 1.82 m, as shown in Figure 10d, the overall change trend of the pressure pulsation (at measuring points P1 and P6) shows the characteristics of first decreasing and then increasing. With the decrease of the *NPSHa*, the uneven distribution of the cavitation area on the three blades deepens; cavitation has become the main factor of the pressure pulsation at this time.

3.5.2. Frequency Domain Analysis

To analyze the frequency domain characteristics of inducer pressure fluctuations under different *NPSHa*, Fourier transform was performed on the pressure fluctuation signals collected at measuring points P1, P4, P6, and P7, as shown in Figure 11.

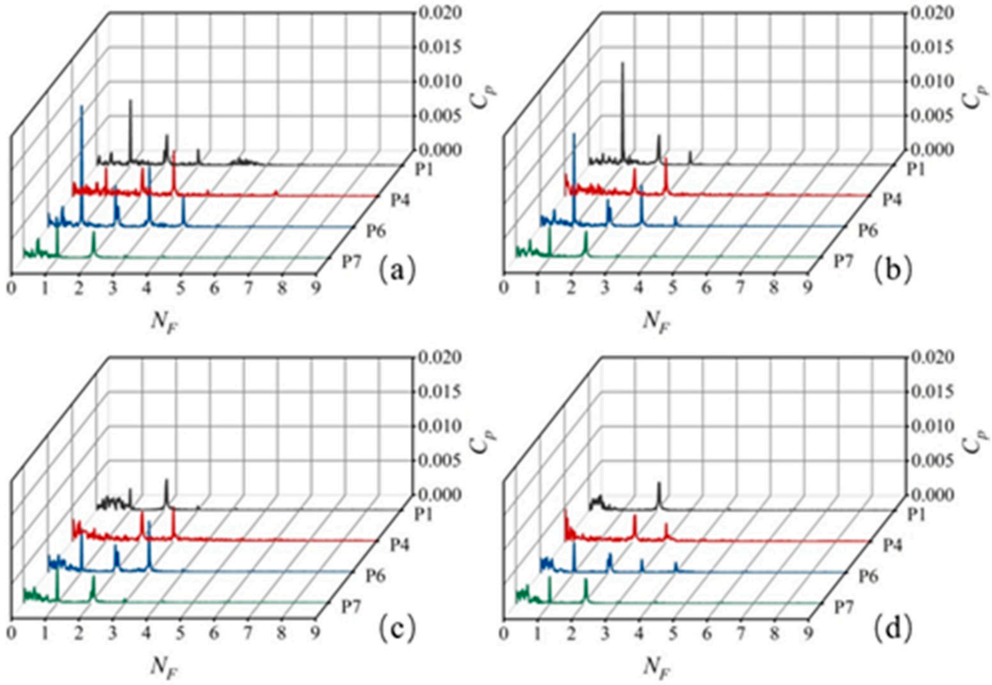

Figure 11. Frequency domains of pressure fluctuations under different *NPSHa.* (**a**) *NPSHa* = 5.51 m, (**b**) *NPSHa* = 4.28 m, (**c**) *NPSHa* = 3.05 m, (**d**) *NPSHa* = 1.82 m.

It can be seen from the figure that when the *NPSHa* is high (5.51 and 4.28 m), the main frequencies at measuring points P1, P6, and P7 are all one-time the shaft frequency, while the main frequency at measuring point P4 is three-times the shaft Frequency. This is quite different from the frequency domain characteristics under the non-cavitation condition. Under the non-cavitation condition, the main frequency at each measuring point is three times the shaft frequency. It shows that after the occurrence of cavitation, the incentive effect of the inducer on pressure pulsation is gradually replaced by the cavitation incentive. With the decrease of the *NPSHa*, the pressure pulsation amplitudes at inlet P1 and outlet P6 of the inducer gradually decrease, and the main frequency positions at the two measuring points also change. When the *NPSHa* is 3.05 m, the main frequency at measuring point P1 is twice the shaft frequency, and the main frequency at measuring point P6 is three times the shaft frequency. When the *NPSHa* is 1.82 m, the main frequency position at the measuring point P6 shifts from three times the shaft frequency to one-time the shaft frequency. In addition, for measuring points P1 and P6, when the *NPSHa* is high, the shaft frequency and its higher-order harmonics can be clearly observed, and both have large amplitudes. When the *NPSHa* decreases, especially when the *NPSHa* is 1.82 m, the amplitude of the shaft frequency and its higher-order harmonics at measuring point P1 drop rapidly, at two times the shaft frequency. However, in the low-frequency part (that is, the part lower than the shaft frequency), there are many low-frequency signals, and the low-frequency pulsation is very strong, indicating that the cavitation in the inlet area of the inducer is serious at this time, and a large number of cavitation bubbles are generated and collapsed in this area, becoming the main source of pulsation excitation.

To analyze the frequency domain characteristics of the pressure pulsation at the inlet of the inducer under different flow conditions when cavitation occurs, the frequency domain characteristics of the pressure pulsation at the measuring point P1, when the *NPSHa* is 1.82 m under three working conditions (0.6 Q_d, 1.0 Q_d, and 1.1 Q_d, respectively), is illustrated in Figure 12. Comparing and analyzing the pressure fluctuation frequency distribution characteristics under the three flow conditions—it can be found that the dominant frequency in the three flow conditions is not the leaf frequency, and the amplitude corresponding to the leaf frequency is very small. It can be basically ignored in design flow conditions and large flow conditions, indicating that cavitation has a major role in the excitation of pressure pulsations at this time. In addition, it can be clearly observed that as the flow rate decreases, the low-frequency signal pulsation below one-time the shaft frequency gradually increases. In 1.0 Q_d and 1.1 Q_d flow conditions, the low-frequency signal pulsation is weak, and its amplitude is much smaller than the amplitude corresponding to two times the shaft frequency. In the 0.6 Q_d flow condition, the pulsation of the low-frequency signal is significantly enhanced, and its amplitude is much greater than the amplitude corresponding to two times the shaft frequency, indicating that the cavitation area has developed to the upstream area of the inducer at this time, and the measurement point P1 is completely in the cavitation area. With the continuous generation and collapse of a large number of bubbles in the cavitation zone, the pressure pulsation amplitude at the measuring point P1 rises sharply. The type of cavitation that causes this low-frequency signal pulsation to be significantly enhanced is defined as recirculation vortex cavitation.

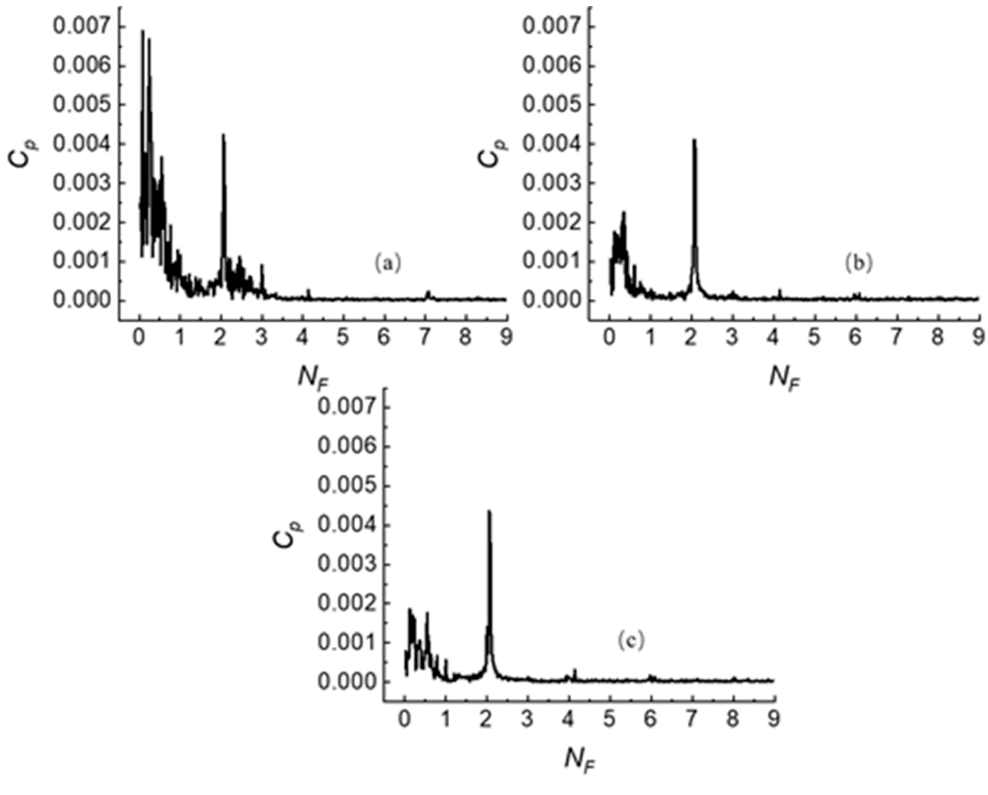

Figure 12. Frequency domains of the inlet pressure fluctuation under different flow rates (**a**) 0.6 Q_d, (**b**) 1.0 Q_d, (**c**) 1.1 Q_d.

3.6. High-Speed Photography Experiment Analysis

To study the cavitation characteristics in the inducer under different working conditions, high-speed photography at 0.6 Q_d, 1.0 Q_d, and 1.1 Q_d flow conditions with *NPSHa* of 5.51, 4.28, 3.05, and 1.82 m were employed, as shown in Figure 13.

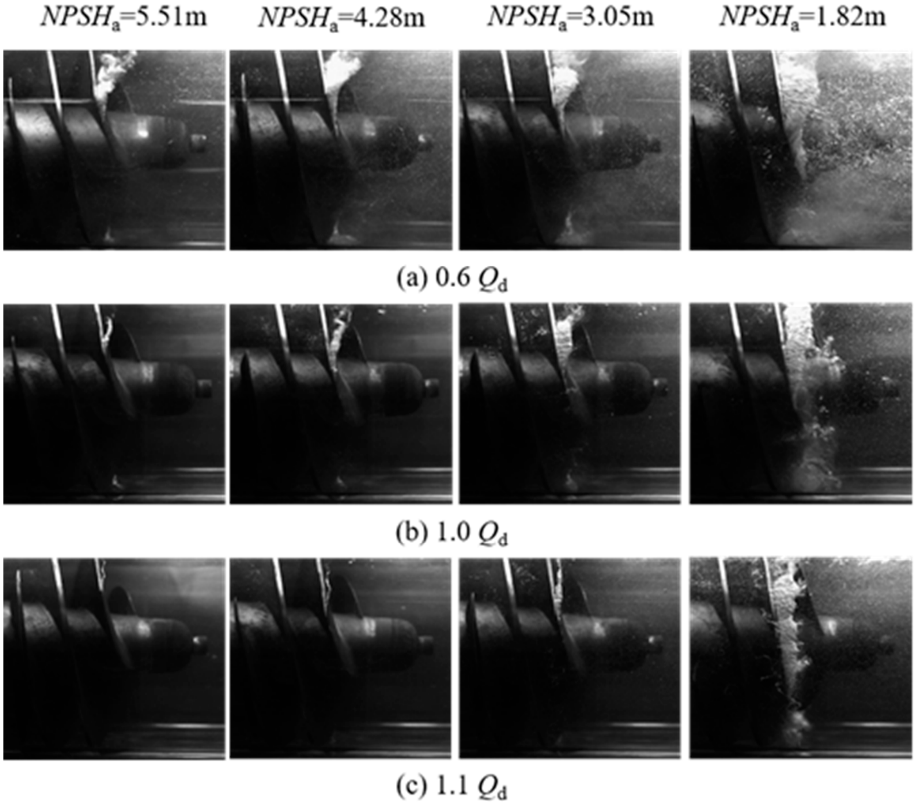

Figure 13. Comparison of cavitation shapes at various flow rates and *NPSHa*.

Comparing the development process of cavitation in the three flow conditions—it can be found that cavitation first appears in the rounded part of the leading edge of the inducer blade. As the *NPSHa* decreases, the degree of cavitation gradually increases, and the number of cavitation bubbles increases rapidly and develops rapidly from the leading edge of the inducer to the trailing edge of the inducer. The volume and distribution area of the cavitation bubbles increase significantly.

The inducer structure adopts an open design, and there is a certain gap between the tip of the blade and the wall of the runner chamber, resulting in a tip leakage vortex. When the pressure at the center of the vortex is low, the tip leakage vortex cavitation is formed as shown by the high-speed photography results at 1.0 Q_d and *NPSHa* = 5.51 m. When the *NPSHa* decreases to 4.28 m, the circumferential length of the tip leakage vortex cavitation increases significantly, and the tail region of the leakage vortex presents a band-like distribution. The cavitation area of the entire leakage vortex rapidly decreases and disappears along the direction opposite to the rotation direction of the inducer. At the same time, the tail is accompanied by obvious shedding and oscillation phenomenon. When the *NPSHa* is 3.05 m, a sheet-like shear layer cavitation is developed from the tip leakage vortex and perpendicular to the blade surface, which connects the tip leakage vortex and the gap cavitation to form a triangular cavitation cloud. When the *NPSHa* is 1.82 m, the rim of the suction surface of the inducer is covered by the cavitation cloud, the upstream area is also full of cavitation, and the degree of cavitation has been very serious.

Comparing the development of the cavitation area in different flow conditions under the same *NPSHa*, it can be found that under the same *NPSHa*, the cavitation area in small flow conditions is larger and the degree of cavitation is more serious. When the *NPSHa* is 5.51 m, the cavitation area only occurs in a small area near the tip of the blade under the high flow rate of 1.1 Q_d. It is in the shape of a slender ribbon, which is called a vortex filament, and the shape is not easily observed. In the design flow rate of 1.0 Q_d, the length of the cavitation vortex has developed, and its diameter is significantly larger than that in the high flow rate, so its morphological characteristics can be easily captured. When the flow rate is further reduced to 0.6 Q_d, the cavitation vortex develops into a cavitation cloud cluster. It can be seen that this cloud-like cavitation has significant unsteady characteristics, and a large number of shedding cavitation bubbles appear at the tail of the cavitation area. The above phenomenon shows that cavitation is more likely to occur in the inducer under small flow conditions, and the development speed of the cavitation is faster, resulting in a rapid deterioration of the flow state at the inlet.

Figure 14 shows the morphological characteristics of the cavitation areas at different times in the three flow conditions of 0.4 Q_d, 1.0 Q_d, and 1.1 Q_d. It can be found that in the low flow rate of 0.4 Q_d, the tip leakage vortex cavitation, shear layer cavitation, and gap cavitation constitute a large range of triangular cavitation clouds. When t = 0, the tail of the triangular cavitation cloud cluster appears to fall off. When t = 2.5 ms, the circumferential length of the cavitation cloud cluster decreases, and the shape is elongated. In addition, a shed cavitation cloud cluster appears at the tail of the main cavitation cloud cluster. When t = 5 ms, the second shedding cloud cluster appears, and the volume of the first cavitation cloud cluster is greatly reduced. This is due to the effect of viscosity, which causes the cavitation cloud cluster to continuously dissipate energy when rotating with the blade. In the design flow 1.0 Q_d working condition, with the same cavitation margin, the tip leakage vortex cavitation did not yet develop into cloud cavitation, and there are two spiral cavitation wakes in the cavitation tail region, such as t = 2.5 ms, as shown in the image. This is because the periphery of the leakage vortex is curled under the action of shear stress, causing the entire leakage vortex to continuously revolve around itself, so the cavitation wake appears as a spiral motion. In the high flow rate of 1.1 Q_d, severe rim cavitation occurs, and the entire blade tip area is covered by large-volume cavitation clouds, but the coverage area of the cavitation clouds is relatively stable. With time, the cavitation cloud cluster does not see major changes. At t = 5 ms, two spiral cavitation wakes also appear at the tail of the vacuole cloud. Based on the above analysis, it can be concluded that in the small flow condition, the cavitation area has a larger distribution range, more severe instability characteristics, and the flow state is more likely to deteriorate.

Figure 15 shows the evolution characteristics of the tip vortex cavitation at the inlet of the inducer in the design flow of 1.0 Q_d. When the *NPSHa* is 3.05 m as shown in Figure 15a, in addition to the main vortex structure, there is also a spiral cavitation vortex at the tail of the tip leakage vortex. The length of the cavitation vortex is not a fixed value. It increases with the rotation of the inducer. However, due to the effect of viscous dissipation, the strength of the cavitation vortex continues to decrease. When t = 2.5 ms, the gradually disappearing cavitation vortex is entrained by the leading edge of the next blade, and its strength rises again after being supplemented by energy, forming a vortex structure perpendicular to the suction surface of the blade. At this time, the part of the vertical cavitation vortex attached to the surface of the blade is stronger and more obvious, while the part above the surface of the blade is weaker and distributed in small bubbles. When t = 5 ms, the part of this vertical cavitation vortex located on the surface of the blade merges with the tip leakage vortex, the part above the blade is entrained by the tip leakage vortex, and its strength increases rapidly. When t = 7.5 ms, the second vertical cavitation vortex appears on the leading edge of the blade, and the diameter of the vortex band of the first vertical cavitation vortex significantly reduces due to viscous dissipation. When the *NPSHa* is 1.82 m as shown in Figure 15b, due to the decrease of inlet pressure, the degree of cavitation in the inducer increases, and the area of cavitation increases significantly. When t = 0 ms, the cavitation vortex at the tail of the tip leakage vortex develops into a cavitation cloud cluster, and separates from the tip leakage vortex at t = 2.5 ms. The rotation speed of the shedding vortex structure is significantly lower than the rotation speed of the inducer. After that, it is cut off by the leading edge of the next blade, and one part moves to the pressure surface of the blade. It is squeezed by the high-pressure liquid and collapsed, aggravating the instability of the flow, while the other part is affected by the tip leakage vortex of the next blade. The entrainment effect of the vortex structure rapidly increases the volume of the vortex structure and interacts with the cavitation zone of the blade tip to deepen the cavitation in this zone.

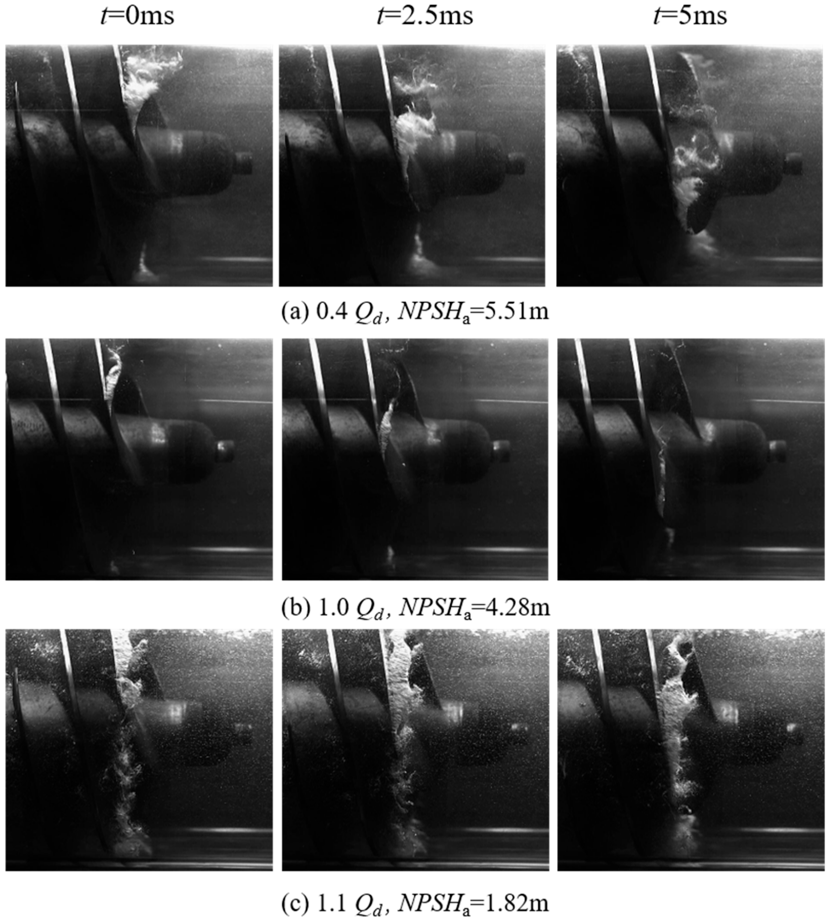

Figure 14. Evolution of cavitation under different conditions.

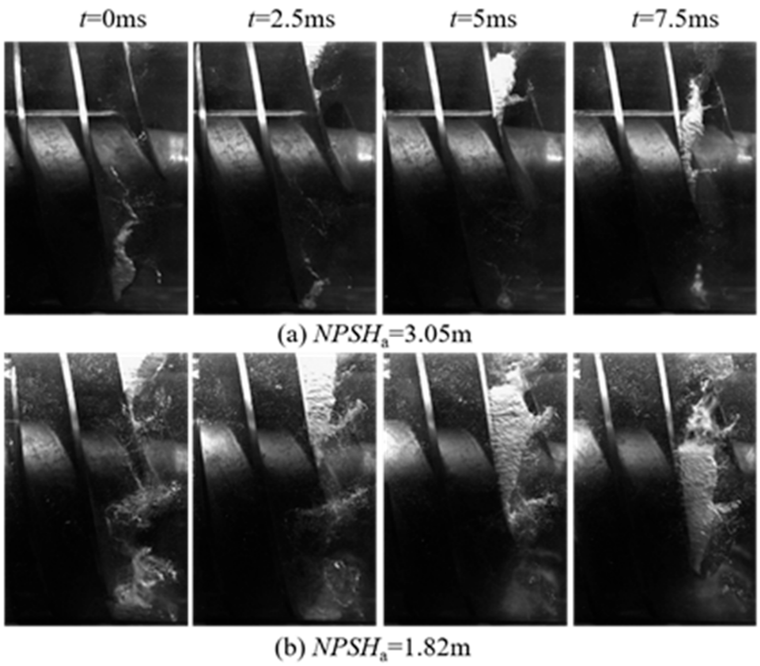

Figure 15. Evolution of the structure of the tip vortex cavitation under different *NPSHa*.

4. Conclusions

In this paper, we conducted a series of experimental studies on an inducer, including an external characteristic experiment, a cavitation performance experiment, a pressure pulsation experiment, and a high-speed photography experiment under cavitation and non-cavitation conditions. The following conclusions obtained from this study can be summarized as follows:

(1) Under non-cavitation conditions, the change in the flow rate has a significant impact on the pressure pulsation characteristics in the inducer. For the pressure pulsation signals at the measuring points located at the inlet, middle, and outlet of the inducer, the crest and valley numbers in a cycle are the same as the blade numbers of the inducer. In addition, there is strong periodicity in the 1.0 Q_d working condition, weaker periodicity in the partial working condition, and a large number of secondary peaks.

(2) The cavitation occurrence aggravated the instability of the flow and caused the intensity of the pressure pulsation at each measuring point to increase. As the *NPSHa* continues to decrease, the amplitude corresponding to the frequency higher than the shaft frequency in the frequency domain diagram gradually decreases. The main frequency at each measurement point moves to the low-frequency signal, and the low-frequency signal takes the dominant position. Under the same *NPSHa*, as the flow rate decreases, the number of low-frequency signals and the corresponding amplitude increase significantly, which is consistent with the frequency domain change characteristics under non-cavitation conditions.

(3) Comparing and analyzing the results of high-speed photography in different working conditions—it is found that cavitation first appears in the tip area of the inducer. As the *NPSHa* decreases, the cavitation area rapidly expands and the cavitation develops from the tip leakage vortex cavitation to a triangular cavitation cloud. This cavitation structure has strong instability, and the tail region is often accompanied by shedding cavitation clouds perpendicular to the blade surface. Under the same *NPSHa*, the cavitation in the small flow condition occurs earlier, the cavitation area is larger, and the flow state deteriorates faster.

(4) Under the design flow condition, with the decrease of the cavitation margin, the vertical cavitation vortex induced by the tip leakage vortex and the tail shedding significantly increase in intensity and size. In the smaller cavitation margin, the vertical cavitation vortex stays in the flow field for a long time, aggravating the cavitation at the tip of the inducer, and affecting the work and stable operation of the inducer seriously.

Author Contributions: Conceptualization, H.W. and J.F.; methodology, J.F.; software, K.L.; validation, H.W., X.S. and B.X.; formal analysis, X.S.; investigation, H.W.; resources, J.F.; data curation, J.F.; writing—original draft preparation, H.W.; writing—review and editing, B.X. and W.Z.; visualization, J.F.; supervision, B.X.; project administration, B.X.; funding acquisition, B.X. and D.Z. All authors have read and agreed to the published version of the manuscript.

Funding: This research was funded by the National Natural Science Foundation of China (No. U2106225), the Outstanding Youth Foundation of Jiangsu Province of China (No. BK20211547), Natural Science Foundation of Jiangsu Province (21KJA470002), the Senior Talent Foundation of Jiangsu University (No. 18JDG034), and the Postdoctoral Science Foundation of Jiangsu Province (No. 2018K102C).

Institutional Review Board Statement: Not applicable.

Informed Consent Statement: Not applicable.

Data Availability Statement: Not applicable.

Acknowledgments: The authors would like to thank the editors and the anonymous reviewers for their helpful and constructive comments. Their time is precious and the relevance of the comments on our manuscript mean that they have dedicated a significant portion of it to help us improve our work.

Conflicts of Interest: The authors declare no conflict of interest.

References

1. Xi, Y.; Wang, N.; Li, J.; Zhang, Z.; Han, L. Experimental and numerical study on pressure oscillation in a combustor with rotary valve. *Chin. J. Aeronaut.* **2021**, *34*, 298–314. [CrossRef]
2. Ren, P.; Wang, H.; Zhou, G.; Li, J.; Cai, Q.; Yu, J.; Yuan, Y. Solid rocket motor propellant grain burnback simulation based on fast minimum distance function calculation and improved marching tetrahedron method. *Chin. J. Aeronaut.* **2020**, *34*, 208–224. [CrossRef]
3. Li, Y.; Fang, J.; Sun, B.; Li, K.; Cai, G. Index allocation for a reusable LOX/CH4 rocket engine. *Chin. J. Aeronaut.* **2021**, *34*, 432–440. [CrossRef]
4. Tian, H.; Duan, Y.; Zhu, H. Three-dimensional numerical analysis on combustion performance and flow of hybrid rocket motor with multi-segmented grain. *Chin. J. Aeronaut.* **2020**, *33*, 1181–1191. [CrossRef]
5. Song, A.; Wang, N.; Li, J.; Ma, B.; Chen, X. Transient flow characteristics and performance of a solid rocket motor with a pintle valve. *Chin. J. Aeronaut.* **2020**, *33*, 3189–3205. [CrossRef]
6. Wang, C.; Zhang, X.; Gao, Y.; Chen, H. Investigation on Schemes for Accelerating Oxidizer Boost Pump During Start-Up of LOX/Kerosene Staged Combustion Rocket Engine. *J. Propulsion Technol.* **2020**, *41*, 1441–1448.
7. Li, D.; Ren, Z.; Li, Y.; Gong, R.; Wang, H. Thermodynamic effects on the cavitation flow of a liquid oxygen turbopump. *Cryogenics* **2021**, *116*, 103302. [CrossRef]
8. Zhai, L.; Li, Y.; Cui, B.; Guo, J.; Li, X.; Zhu, Z. Studies of cavitation characteristics of inducers with different blade numbers. *AIP Adv.* **2021**, *11*, 085216. [CrossRef]
9. Guan, X.-Y.; Jia, B.-Q.; Yang, L.-J.; Fu, Q.-F. Linear instability of an annular liquid jet with gas velocity oscillations. *Phys. Fluids* **2021**, *33*, 054110. [CrossRef]
10. Rutard, N.; Dorey, L.-H.; Le Touze, C.; Ducruix, S. Large-eddy simulation of an air-assisted liquid jet under a high-frequency transverse acoustic forcing. *Int. J. Multiph. Flow* **2019**, *122*, 103144. [CrossRef]
11. Chen, T.; Mu, Z.; Huang, B.; Zhang, M.; Wang, G. Dynamic instability analysis of cavitating flow with liquid nitrogen in a converging–diverging nozzle. *Appl. Therm. Eng.* **2021**, *192*, 116870. [CrossRef]
12. Zhang, S.; Chen, H.; Ma, Z. A modified filter-based model for simulation of unsteady cavitating flows around a NACA66 hydrofoil. *Mod. Phys. Lett. B* **2020**, *35*. [CrossRef]
13. Yu, J.; Liu, J.-H.; Wang, H.-K.; Wang, J.; Zhang, L.-P.; Liu, G.-Z. Numerical simulation of underwater explosion cavitation characteristics based on phase transition model in compressible multicomponent fluids. *Ocean Eng.* **2021**, *240*, 109934. [CrossRef]
14. Li, Y.; Deng, J. Numerical investigation on the performance of transcritical CO2 two-phase ejector with a novel non-equilibrium CFD model. *Energy* **2021**, *238*, 121995. [CrossRef]
15. Kim, H.; Kim, C. A physics-based cavitation model ranging from inertial to thermal regimes. *Int. J. Heat Mass Transf.* **2021**, *181*, 121991. [CrossRef]
16. Bermejo, D.; Escaler, X.; Ruíz-Mansilla, R. Experimental investigation of a cavitating Venturi and its application to flow metering. *Flow Meas. Instrum.* **2021**, *78*, 101868. [CrossRef]
17. Lee, K.-H.; Yoo, J.-H.; Kang, S.-H. Experiments on cavitation instability of a two-bladed turbopump inducer. *J. Mech. Sci. Technol.* **2009**, *23*, 2350–2356. [CrossRef]
18. Kim, J.; Song, S.J. A water test facility for a turbopump inducer cavitation experiment. In Proceedings of the 15th International Symposium on Transport Phenomena and Dynamics of Rotating Machinery (ISROMAC), Honolulu, HI, USA, 1 January 2014.
19. Cui, B.; Chen, J.; Li, X.; Lin, Z.; Cai, H.; Han, A. Experiment and Numerical Simulation of Cavitation Evolution in High Speed Centrifugal Pump with Inducer. *Trans. Chin. Soc. Agric. Machin.* **2018**, *49*, 148–155.
20. Cui, B.; Chen, J. Visual experiment and numerical simulation of cavitation instability in a high-speed inducer. *Proc. Inst. Mech. Eng. Part A J. Power Energy* **2019**, *234*, 470–480. [CrossRef]
21. Li, L.; Ding, Z.; Zhou, L.; Wu, Y. An Experiment on Cavitating Flow in Rocket Engine Inducer. *Trans. Nanjing Univ. Aeronaut. Astronaut.* **2019**, *36*, 306–312.
22. Xiang, L.; Chen, H.; Tan, Y.; Xu, K.; Liu, J. Experiment of Cavitating Flow Characteristics of Inducer. Trans. *Chinese Soc. Agric. Machin.* **2019**, *50*, 125–132.
23. Zhang, Y.H.; Chen, H.; Xiang, L.; Chen, W.; Xu, K.; Li, Y. Study on Cavitation Performance of Inducer Based on Orthogonal Experiment. *J. Propuls. Technol.* **2020**, *41*, 343–352.
24. Cheng, X.; Yang, D.; Lu, X. Studying on the influence of the annular groove position on the cavitation performance of high-speed inducer. *J. Braz. Soc. Mech. Sci. Eng.* **2021**, *43*, 1–13. [CrossRef]
25. Xu, Z.F.; Kong, F.Y.; Zhang, H.L.; Zhang, K.; Wang, J.Q.; Qiu, N. Research on Visualization of Inducer Cavitation of High-Speed Centrifugal Pump in Low Flow Conditions. *J. Mar. Sci. Eng.* **2021**, *9*, 1240. [CrossRef]
26. Huan, Y.Y.; Liu, Y.Y.; Li, X.J.; Zhu, Z.C.; Qu, J.T.; Zhe, L.; Han, A.D. Experimental and numerical investigations of cavitation evolution in a high-speed centrifugal pump with inducer. *J. Hydrodyn.* **2021**, *33*, 140–149. [CrossRef]
27. Zhang, H.; Xia, B.; Kong, F.Y.; Li, G.D.; Cao, P.Y. Experimental investigation of cavitation characteristics for a high-speed inducer with a great flow rate. *Adv. Mech. Eng.* **2022**, *14*, 1–15. [CrossRef]